NANO LETTERS

pubs.acs.org/NanoLett

Letter

In Vivo High-Contrast Biomedical Imaging in the Second Near-Infrared Window Using Ultrabright Rare-Earth Nanoparticles

Rong Xu, Jiantao Liu, Huiqun Cao,* Danying Lin, Xian Chen, Fuhong Han, Xiaoyu Weng, Yiping Wang, Liwei Liu, Bin Yu,* and Junle Qu*

Cite This: *Nano Lett.* 2023, 23, 11203−11210

Read Online

ACCESS | Metrics & More | Article Recommendations | Supporting Information

ABSTRACT: Intravital luminescence imaging in the second near-infrared window (NIR-II) enables noninvasive deep-tissue imaging with high spatiotemporal resolution of live mammals because of the properties of suppressed light scattering and diminished autofluorescence in the long-wavelength region. Herein, we present the synthesis of a downconversion luminescence rare-earth nanocrystal with a core−shell−shell structure ($NaYF_4$@NaYbF_4:Er,Ce@$NaYF_4$:Ca). The structure efficiently maximized the doping concentration of the sensitizers and increased Er^{3+} luminescence while preventing cross relaxation. Furthermore, Ce^{3+} doping in the middle layer efficiently limited the upconversion pathway and increased downconversion by 24-fold to produce bright 1550 nm luminescence under 975 nm excitation. Finally, optimizing the inert shell coating of $NaYF_4$:Ca and liposome encapsulation reduced the luminescence quenching impact by water and improved biological metabolism. Thus, our synthesized biocompatible, ultrabright NIR-II probes provide high contrast and resolution for through-scalp and through-skull luminescence imaging of mice cerebral vasculature without craniotomy as well as imaging of mouse hindlimb microvessels.

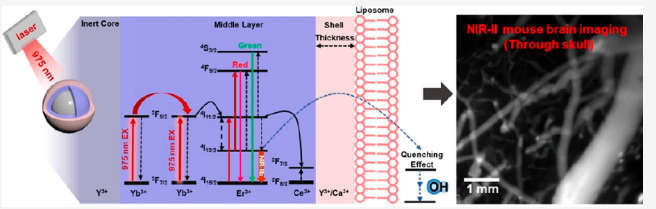

KEYWORDS: *lanthanide nanoparticles, enhancement of the second near-infrared luminescence, liposomes, brain vascular imaging, microvascular imaging*

Diverse preclinical animal models enable the delineation of physiological and pathological systems and provide essential platforms for the development of novel therapeutic techniques. Intravital noninvasive luminescence imaging technology can directly monitor biological processes in real-time (30 frames/s) down to the cellular level because of the high spatial and temporal resolution.[1,2] One-photon luminescence imaging in the visible (400−700 nm) and traditional near-infrared (NIR-I, 750−900 nm) regions of the electromagnetic spectrum; however, from poor resolution for deep-tissue structures and physiological dynamics. Consequently, luminescence at 900−1700 nm (known as the second near-infrared window, NIR-II), which suppresses scattering and reduced autofluorescence, has recently been employed to improve the quality of in vivo luminescence imaging. Notably, the near-infrared IIb window (NIR-IIb, 1500−1700 nm) exhibits virtually no tissue autofluorescence and reduced light scattering, allowing for ultrahigh spatial resolution.[3,4] Furthermore, the 1600 nm spectral region is located in a narrow valley of the water absorption spectrum, where the minimal photon absorbance between the first and second overtones of water allows for deep-tissue access.[1] NIR-IIb has outstanding optical properties, allowing for desirable imaging quality and tissue penetration depth to provide early illness detection, therapy, and prognostic evaluation.[5−9]

Given the advantages of NIR-II, a number of probes have been designed for in vivo imaging and include single-walled carbon nanotubes (SWCNTs), conjugated polymers, organic small molecular dyes, and inorganic-based nanoparticles (NPs) of quantum dots (QDs), and lanthanide-doped NPs (LnNPs).[1,3,10−13] For imaging of mouse brain vasculature, SWCNTs with excitation at 808 nm and emission beyond 1500 nm were developed.[3] QDs are a promising alternative possibility for NIR-IIb probes because of their high luminescence quantum yield (LQY), tunable emission band, and ultrasmall size.[14] Unfortunately, the constituent materials for recently developed NIR-IIb QDs are mainly limited to indium arsenide or lead sulfide/selenide and mercury telluride, limiting the probes to in vivo uses.[10] Wang et al. recently developed gold-doped silver telluride QDs with an NIR-IIb emission band that can efficiently avoid heavy-metal ions.[8] However, this probe is still in the early stages of development, and its biological toxicity needs to be confirmed.

Received: September 26, 2023
Revised: November 17, 2023
Accepted: November 17, 2023
Published: November 21, 2023

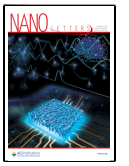

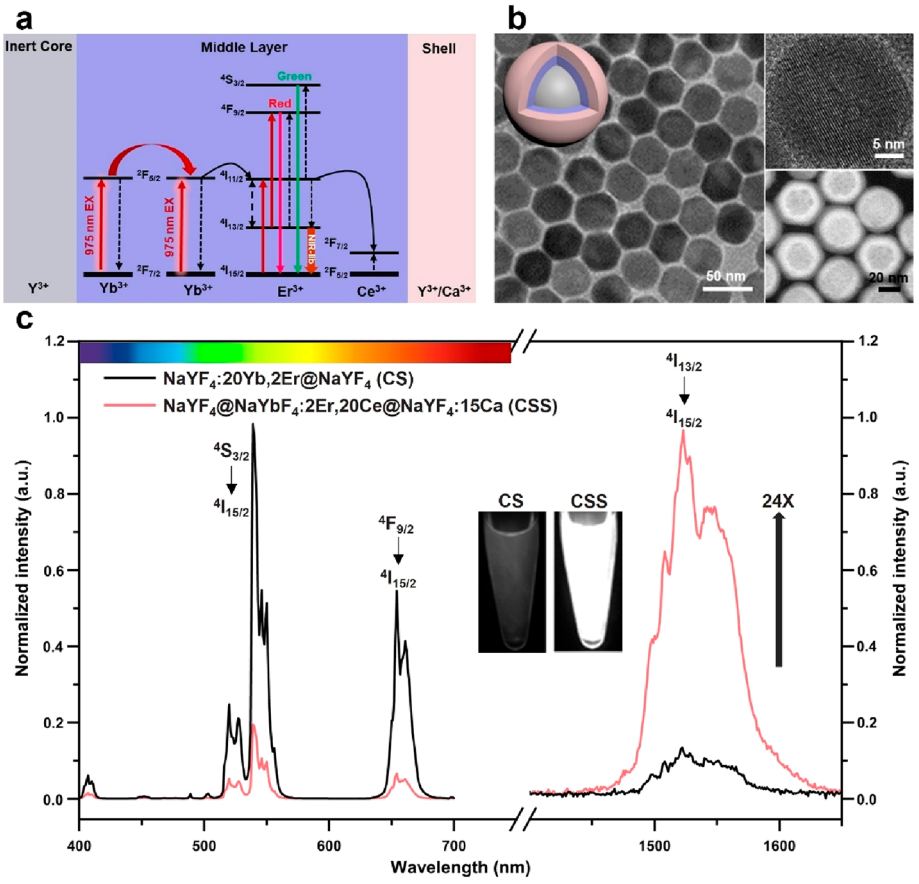

Figure 1. (a) Schematic of the CSS (core−shell−shell) structured Er^{3+} based NIR-IIb probes. (b) TEM, HRTEM, and AC-HAADF-STEM of the synthesized CSS $NaYF_4$@$NaYbF_4$:2Er,20Ce@$NaYF_4$:15Ca. (c) Comparison of the emission intensities of $NaYF_4$@$NaYbF_4$:2Er,20Ce@$NaYF_4$:15Ca and $NaYF_4$:20Yb,2Er@$NaYF_4$ nanoparticles under 975 nm laser excitation, the power density is 1w/cm^2. The inset image displays NIR-IIb imaging results of the two nanoparticles, as acquired by an InGaAs camera with a 1300 nm long pass (LP) filter after excitation by a 975 nm laser.

LnNP probes, which are well-known for their upconversion (UC) luminescence, have recently garnered attention in biological imaging applications because of their low toxicity, narrow band emission, and superior photochemical stability.[15] As an alternative, erbium-doped NPs (Er-LnNPs) exhibit useful downconversion (DC) luminescence properties in the NIR-IIb (1550 nm) region. Er-based LnNPs with NIR-IIb emission peaks have been employed in angiography, tumor targeting, and surgical navigation.[5,16−18] However, the forbidden f−f transitions of rare-earth ions result in a relatively low absorption efficiency of Er^{3+} based LnNPs. Although a high concentration of lanthanide dopants was shown to increase the luminescence intensity by increasing the capacity to sustain excitation energy, this also increased the energy migration through the crystal lattice, depleting the excitation energy.[19] Furthermore, UC and DC are two competing processes in Er^{3+}-based LnNPs that significantly weaken NIR-IIb luminescence, and the DC emission of Er^{3+} ions may be quenched further after transferring to aqueous solutions owing to the high energy transfer between Er^{3+} and OH− groups in solution.[20] Er-LnNPs, like most inorganic NPs, will be retained within the reticuloendothelial system (RES) for an extended period before being cleared, raising safety concerns and limiting their clinical applications.

Herein, we rationally designed and fabricated a versatile Er-based NIR-IIb nanoprobe with a core−shell−shell structure (CSS) termed $NaYF_4$@$NaYbF_4$:Er,Ce@$NaYF_4$:Ca. In this design, a nanoscale $NaYbF_4$ lattice maximizes the sensitizer concentration and then accumulates the excitation energy. By confining the $NaYbF_4$ lattice to the middle shell layer, it suppresses ion cross relaxation and long energy migration, effectively avoiding energy loss in the crystal lattice and enhancing both UC/DC processes. Furthermore, Ce doping in the middle layer efficiently suppresses the UC pathway of Er^{3+} and boosts the NIR-IIb emission. The aqueous quenching impact was also reduced by adjusting the thickness of the $NaYF_4$:Ca inert shell, and the morphology of the NPs was refined by the addition of Ca^{3+}. In aqueous solution, the resulting Er-based LnNPs produced ultrabright NIR-IIb emission. Furthermore, we coated the NIR-IIb Er-based LnNPs with liposomes to address the toxicity issue and accelerate probe clearance. In NIR-IIb, our bright Er-based LnNPs enabled microangiography of mouse hindlimbs as well as noninvasive imaging of mouse brains through the skull and scalp.

The Er-based LnNPs exhibited amplified luminescence at 1550 nm and were composed of a $NaYF_4$ core, a middle shell layer of $NaYbF_4$:2Er,20Ce, and an inert protection layer of $NaYF_4$:15Ca (Figure 1a). The NPs were synthesized using a coprecipitation method where rare-earth acetates were coreacted with oleic acid, 1-octadecene, and/or oleyl amine to yield a uniform NP morphology and narrow size

https://doi.org/10.1021/acs.nanolett.3c03698
Nano Lett. 2023, 23, 11203−11210

distribution.[21] The method has the advantages of low cost, simple operation, and easier preparation of nanoparticles with a uniform morphology. This was confirmed via transmission electron microscopy (TEM) (Figures S1 and S4), which verified that the synthesized spherical $NaYF_4$ core NPs had a highly uniform morphology with size of 18 nm (Figures S2 and S5). The CSS $NaYF_4$@$NaYbF_4$:2Er,20Ce@$NaYF_4$:15Ca NPs were 31 nm in diameter after layer-by-layer shell growth (Figure 1b). High-resolution TEM (upper right of Figure 1b) and X-ray powder diffraction (Figures S3 and S6) confirmed that the synthesized NPs had a single-crystalline structure with a hexagonal phase. The morphology and composition of Er-based NPs (bottom right corner of Figure 1b) were examined using aberration corrected high-annular dark-field scanning TEM. The energy dispersive spectroscopy mapping of Er-based NPs (Figures S7 and S8) confirmed the CSS.

We confined Yb^{3+} ions to the middle shell layer of a hexagonal phase $NaYF_4$@$NaYbF_4$:Er@$NaYF_4$:Ca and fixed the concentration of Er^{3+} to 2% to maximize luminescence emission after excitation by a 975 nm laser. The structure uses the matrix material ($NaYF_4$) as the core and confines the sensitizer and luminescent center ions to the intermediate shell layer. Thus, the long-distance energy migration along the Yb sublattice could be hindered and the depletion of excitation energy through energy migration is suppressed. In this regard, the concentration of Yb is inhibited and the highest sensitizer content can be doped without introducing other ions, consequently enhancing the absorption of excitation energy and boosting local excitation energy density. We observed enhanced emissions in both the visible and NIR-IIb spectra when the Yb^{3+} dopants were at 98% (Figure S9). The lack of long-distance energy migration will probably suppress energy loss to the crystal lattice, which blocks luminescence quenching. However, the UC and DC processes are competing in Er^{3+}-based NPs. The energy transfer between Yb^{3+} and Er^{3+} ions in NPs is the underlying mechanism that generates luminescence, whereby Yb^{3+} ions are used as sensitizers to harvest energy at 975 nm by pumping electrons to populate the $^2F_{5/2}$ state of Yb^{3+} and an efficient Yb^{3+}-to-Er^{3+} energy transfer ensures Er^{3+} excitation to the intermediate $^4I_{11/2}$ level (Figure 1a).[19] In the DC process, a short-lived $^4I_{11/2}$ excited state allows for a rapid nonradiative decay into the $^4I_{13/2}$ state, followed by NIR-IIb (1550 nm) emission. We then doped Ce^{3+} ions with only two energy levels into the middle shell layer to shorten the lifetime of the Er $^4I_{11/2}$ state, enhance DC emissions in NIR-IIb, and suppress UC emissions in the visible region. The energy difference between $^2F_{5/2}$ and $^2F_{7/2}$ produces a small mismatch with the energy difference of Er^{3+}, allowing efficient nonradiative cross relaxation in the Er $^4I_{11/2}$ state and significant population of the Er $^4I_{13/2}$ level (Figure 1a).[22] DC emissions were effectively enhanced by optimizing the concentration of Ce^{3+} at 20% (Figure S10). Furthermore, the UC emission of Er-LnNPs at 540 and 654 nm was significantly reduced, owing to the depopulation of the Er $^2H_{11/2}$, $^4S_{3/2}$, and $^4F_{9/2}$ levels in the presence of Ce^{3+} ions. The luminescence lifetimes corresponding to different Ce^{3+} concentrations (Figure S11) revealed that the lifetime of Er^{3+} in the visible region decreased with increasing Ce^{3+} concentration, confirming that the DC pathway can be suppressed with added Ce^{3+}. Importantly, the Yb sublattice should enclosed in an inert protection layer, such as $NaYF_4$:Ca, as the luminescence of the $NaYF_4$@$NaYbF_4$:Er,Ce core−shell structure is weak because of surface quenching.[23,24]

We compared the representative UC and DC emission spectra of $NaYF_4$@$NaYbF_4$:2Er,20Ce@$NaYF_4$:15Ca and conventional $NaYF_4$:20Yb,2Er@$NaYF_4$ NPs upon 975 nm excitation with a continuous wave (CW) laser to validate the imaging performance of the optimized CSS NPs (Figure 1c). The absorption spectra of $NaYF_4$:20Yb,2Er@$NaYF_4$ and $NaYF_4$@$NaYbF_4$:2Er,20Ce@$NaYF_4$;15Ca are shown in Figure S12. After optimizing the Ce^{3+} concentration at 20% and the protection shell coating, the NIR-IIb emission of the Er-LnNPs increased by 24-fold when compared with that of $NaYF_4$:20Yb,2Er@$NaYF_4$. The absolute LQY of $NaYF_4$@$NaYbF_4$:2Er,20Ce@$NaYF_4$:15C in near-infrared region reached 22.7%, detailed testing procedure has been added in Supporting Information. luminescence intensities of the existing Er^{3+}-based LnNPs and our CSS NPs were also compared.[1,25] The NIR-IIb emissions of both the hexagonal and cubic phase $NaYbF_4$:2Er,2Ce@$NaYF_4$ luminescence was lower than those of the CSS NPs (Figure S13), with the magnitude of luminescence of the CSS NPs being 7.3-fold higher than that of β-$NaYbF_4$:2Er,2Ce@$NaYF_4$. This phenomenon occurs because the structure of $NaYbF_4$:2Er,2Ce@$NaYF_4$ may contain additional surface defects that impair the luminescence emission.

To use Er-based NPs in biological applications, the original hydrophobic NPs must be transferred to a water solution. However, the hydroxyl group in water considerably reduces the NIR-IIb luminescence emitted by Er-based LnNPs; a phenomenon attributed to two-photon quenching between $^4I_{13/2}$ and $^4I_{15/2}$ levels of Er^{3+} and the OH− groups of water (Figure 2a). The energy spacing of the $Er^{3+4}I_{13/2}$ to $^4I_{15/2}$ transition for the 1550 nm luminescence is 6500 cm^{-1}, allowing generation quenching by OH− groups with fundamental stretching vibration frequencies ranging from 2700 to 3700 cm^{-1}.[20,26]

The most common way to reduce this aqueous quenching effect is to coat an inert shell to increase the distance between activators and surface quenchers.[27] Typically, an additional inert shell approximately 3 nm thick can protect the UC emission from the quenching effect caused by surface ligands and aqueous solvents. However, when we synthesized a ∼3 nm $NaYF_4$:15Ca shell on the $NaYF_4$@$NaYbF_4$:Er,Ce NPs (Figure 2c), the quenching effect of Er-based NPs was reduced, but significant DC emission losses remained. To suppress surface defects and the two-photon quenching effect of Er^{3+} more completely, we increased the shell thickness from 3 to 9 nm to isolate the Er^{3+} ions in the inert layer of NPs from water (Figure 2b). As the shell thickness increased to 8 nm, the NIR-IIb emission of Er-based NPs in water solution was effectively increased to 5.35-fold that of Er-based NPs with a 3 nm shell (Figure 2c,d). Increases in the thickness of the $NaYF_4$ shell did not provide additional enhancement to the 1550 nm luminescence, which was probably because of the decreased absorption of the excitation light by Yb^{3+} in the core through a thicker shell.

To meet intravital applications, Er-based LnNPs need hydrophilic surfaces for high dispersibility and stability in an aqueous solution. Biocompatibility and biosafety are also critical for in vivo imaging. Nonetheless, the majority of RENPs does not meet the ultrasmall threshold for renal clearance (6−8 nm) to produce persistence in the RES and thus are not quickly cleared during complications.[28] Here, we used liposomes to improve the extractability of RENPs from the RES system (liver and spleen). Liposomes are composed of

https://doi.org/10.1021/acs.nanolett.3c03698
Nano Lett. 2023, 23, 11203−11210

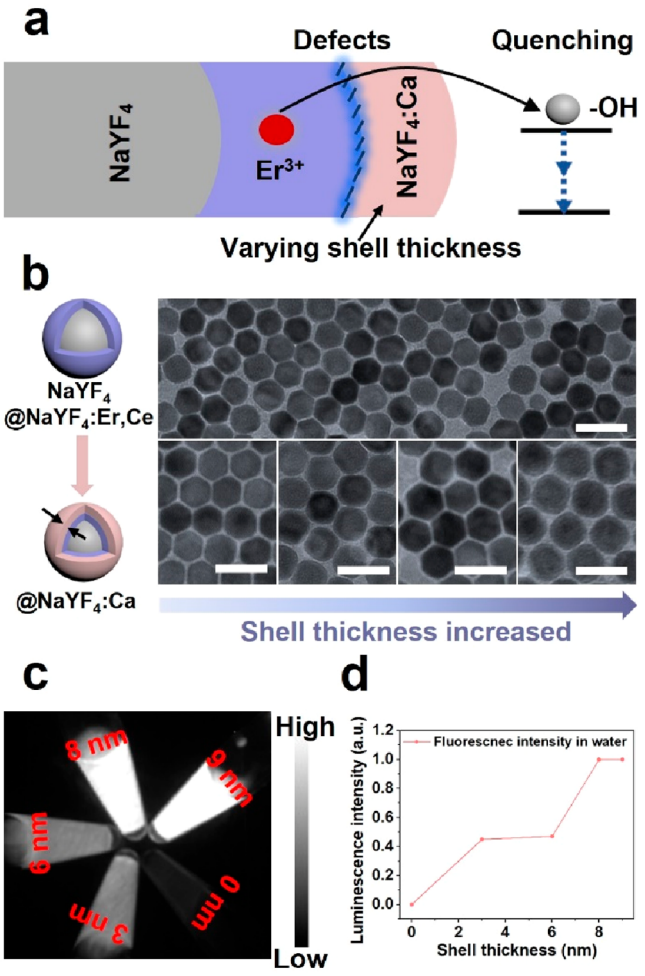

Figure 2. (a) Schematic illustration of the proposed quenching mechanism of CSS structures Er^{3+}-based LnNPs. (b) TEM images of $NaYF_4$@$NaYbF_4$:2Er,20Ce@$NaYF_4$:15Ca under different protection shell thicknesses. (c) Luminescence image of CSS structured nanoparticles with different shell thickness, as acquired by an InGaAs camera with a 1300 nm LP filter after excitation by a 975 nm laser. (d) Variation of luminescence intensity of nanoparticles with different thickness of protection layer.

phospholipid bilayers that have a lipophilic head and hydrophilic tail; this structure is similar to the biological membrane. The natural amphiphilic molecules' composition renders them biocompatible and biodegradable and have consequently been approved by the Food and Drug Administration as drug delivery carriers. More and more works demonstrate that PEGylated liposomes can effectively escape the capture of RES system and excretion of nanoparticles.[29−33] To produce liposomes, we combined 1,2-dipalmitoylphosphatidylcholine (DPPC), cholesterol (Chol), and PEGylated lipid (1,2-distearoyl-*sn*-glycero-3-phosphoethanolamine-*N*-[methoxy-(polyethylene glycol)-2000] (DSPE-PEG2000) at a 77.5:20:2.5 molar ratio.[34] The composition of Er^{3+}-based LnNPs coated with liposomes (abbreviated Er-LnNPs@liposomes) is shown in Figure 3a. According to TEM microscopy (Figure 3b), Er-LnNPs@liposomes had a highly uniform morphology with an average size of 34 nm (a coating thickness of approximately 3 nm). Dynamic light scattering (DLS) measurements (Figure 3c) tracked the variation among Er-based LnNPs with different surface ligands, revealing that the average hydrodynamic diameter (RH) of Er-based LnNPs

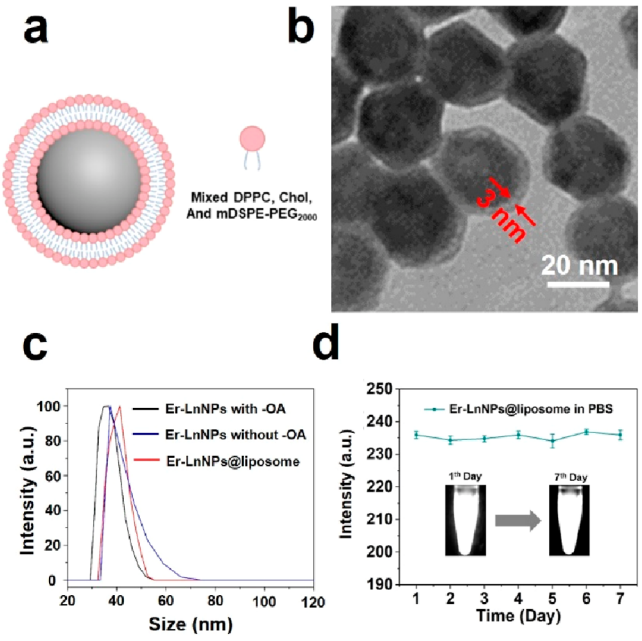

Figure 3. (a) Schematic structure illustration of the Er-LnNPs@liposome. (b) TEM image of the Er-LnNPs@liposome. (c) DLS spectra of hydrophobic Er-LnNPs in cyclohexane, hydrophilic Er-LnNPs in water, and hydrophilic Er-LnNPs@liposome in PBS. (d) NIR-IIb emission intensity of the Er-LnNPs@liposome in 1× PBS of Days. Inset displays 1550 nm luminescence images of LnNPs@liposome in 1× PBS on days 1 and 7.

with/without OA is ∼35 nm and that of Er-LnNPs@liposome is ∼41 nm. Furthermore, evaluation of the photostability of LnNPs@liposomes in PBS with a 975 nm CW laser (200 mW cm^{-2}) revealed that the NIR-IIb luminescence intensity remained constant over 7 days with no decreases (Figure 3d). The excellent aqueous dispersibility due to uniform morphology of nanoparticles and suitable surface modification. In addition, the effective enhancement of NIR-IIb luminescence and natural stability of rare earth doped nanoparticles enable strong photostability of the probes. The validation of physicochemical stability and the evaluation of potential toxicity of the probes can be found in the Supporting Information (Figures S13a,b; S14a,b; S15−S17). In addition, the study of the probe's pharmacokinetics was supplemented in Figures S18−S20.

We then performed in vivo mouse hindlimb vasculature imaging using bright Er^{3+}-based NPs and a 2D InGaAs camera. Probes were excited with a 975 nm laser, and the luminescence at 1550 nm was detected in intravenously injected Er-LnNPs@liposomes (2 mg/mL, 200 μL). The hindlimbs of nude mice were stained with medical indocyanine green (ICG, NIR-I dyes with an emission peak at 835 nm) and Er-LnNPs@liposomes (with an emission peak at 1550 nm) (Figure 4a,b). The imaging results show that the Er-LnNPs@liposomes had a high penetration depth over ICG, with a nearly zero tissue autofluorescence background. The Er-LnNPs@liposomes successfully visualized the vascular structures of mouse hindlimbs and distinguished the closely spaced femoral artery and vein, which are separated by 204 μm (Figure 4c). The ICG, however, was almost completely unable to distinguish between the mouse femoral artery and vein. We quantified the higher spatial resolution and signal-to-background ratio (SBR) of the Er-LnNPs@liposome group and compared them with

https://doi.org/10.1021/acs.nanolett.3c03698
Nano Lett. 2023, 23, 11203−11210

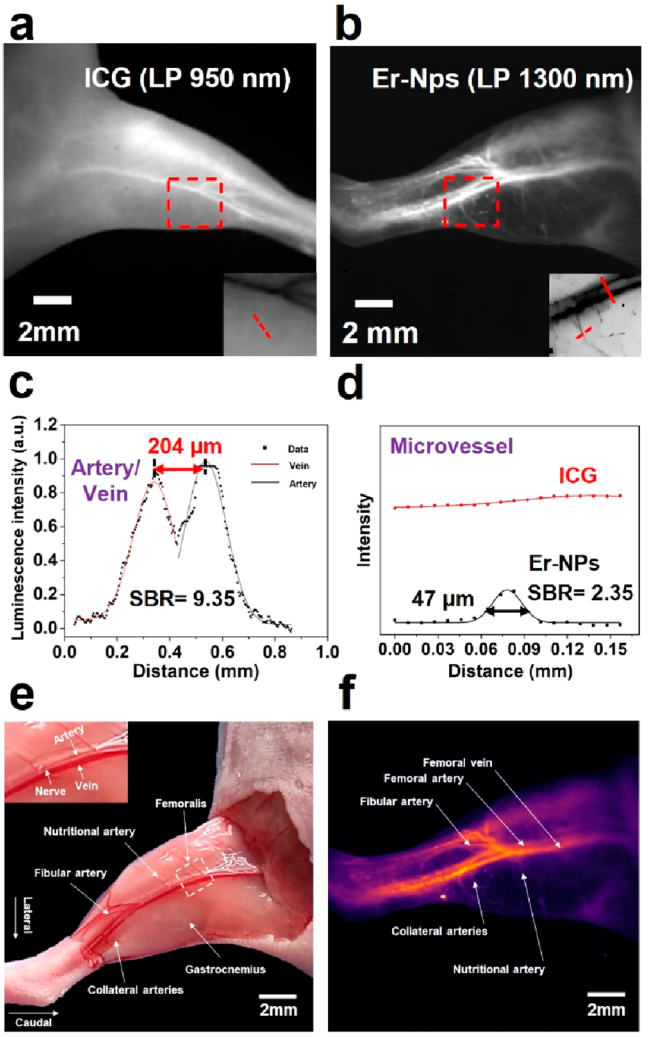

Figure 4. (a) NIR-IIb images of hindlimbs of nude mice with medical ICG (with a 950 nm LP filter) and (b) Er-LnNPs@liposome (with a 1300 nm LP filter). (c) SBR of the NIR-IIb images of the vessel with LnNPs@liposome (see red line in inset picture in panel b). (d) SBR of NIR-IIb images of gastrocnemius microvessels with ICG and LnNPs@liposome (see red dotted line in insets picture in a and b). (e) Illustration of anatomic hindlimb vascular structure. (f) Corresponding NIR-IIb imaging with LnNPs@liposome, displaying deeper tissue with more detail.

those of the ICG group using gastrocnemius microvessel bioimaging (Figure 4d), where the Er-LnNPs@liposomes distinguished a microvessel with a 47-μm width (fwhm). Additional visualizations of the mouse anatomic hindlimb vascular structure using the Er-LnNPs@liposomes are shown in Figure 4e,f. The strong NIR-II luminescence of the probes enables convenient visualization of tiny blood vessels in deep tissue, aiding in the identification of subtle lesions. This makes it possible to apply in vivo microangiography and disease monitoring to conditions such as aberrant neovascularization in tumorigenesis and prognostic monitoring of major disease, due to the excellent optical characteristics and biocompatibility of Er-LnNPs@liposomes.

Simulation of probe penetration depth in vitro has been added in Figure S21, and both 1% intralipid and chicken breast tissue verified the penetration depth of the probe over 4 mm. Taking advantage of the excellent penetration depth of Er-LnNPs@liposomes in vitro, we performed noninvasive in vivo cerebrovascular luminescence imaging of healthy C57Bl/6 mice through intravenously injection of Er-LnNPs@liposomes (2 mg/mL, 200 μL). Without craniotomy, whole mouse heads with hairless scalps were imaged with NIR-IIb under 975 nm CW laser illumination (Figure S23a). Imaging was performed through the intact mouse scalp (Figure 5a,c), and emissions in the inferior cerebral veins, superior sagittal sinus (SSS, at a depth of 1−2 mm under the scalp skin), superficial veins, and transverse sinus could be clearly distinguished with high SBR. After removing the scalp, the blurriness of the background signals and vessels caused by scattering was reduced even further, producing sharper images that clearly revealed the inferior cerebral vein (Figure 5b,c). A homemade stereotactic platform was used to measure microvessel inside the brain by replacing the higher magnificent objective (Figure S23b). Microscopic imaging was performed on the entire mouse head while zooming into the right hemisphere near the location where cortical vessels branch from the SSS (Figure 5d) to observed capillary vessels branching from larger vessels (Figure 5e). A cross-sectional intensity profile of one of the capillary vessels was obtained with a Gaussian-fitted fwhm of 77.62 μm and an SBR of 2.75 (Figure 5f). The microvessel images are blurred because of the relative strong scattering coefficients of the scalp ($\mu = 0.11\lambda^{-4} + 1.61\lambda^{-0.22}$), where the two terms are attributed to Rayleigh and Mie scattering, respectively.[35] We investigated the performance of brain microvessel imaging through the skull, despite this limitation. We obtained the sharpest microvessel images after removing the scalps of the mice heads (Figure 5g,h). A Gaussian-fitted fwhm of 15.21 μm was found in the cross-sectional intensity profile of a capillary vessel through the skull (Figure 5i). Notably, the SBR of brain microvessels beneath the intact skull reached 8.82, which is significantly higher than previous results obtained with other NIR fluorophores.[6,7,16,36]

The CSS Er-based NIR-IIb NPs developed in this study could effectively regulate the photon transition from the $^4I_{13/2}$ to $^4I_{15/2}$ nonradiative transition of Er^{3+}, and high Yb^{3+} concentration reduced the excitation energy from traveling a long distance, allowing significant amplification at 1550 nm. Given the rich and ladderlike energy levels of lanthanide ions, we expect more potential NIR-II probes (e.g., using Ho^{3+} or Tm^{3+}) to be discovered based on existing structures, enriching the available lanthanide-based NPs in the "most-tissue-transparent" NIR-IIb region. By using appropriate inert coatings and liposome surface modification, we developed Er^{3+}-based NPs with a high colloidal stability and favorable biocompatibility. Er-LnNPs@liposomes had intrinsically narrow emission bands. Our NIR-IIb luminescence imaging system enabled high-resolution imaging of mouse hindlimb vascular tissue, with arteries/veins clearly distinguished. We also demonstrated the high NIR-IIb emissions of Er-LnNPs@liposomes by performing noninvasive mouse brain imaging through the intact skin and skull, successfully resolving cerebral vasculatures with a high sub-20 μm spatial resolution and an SBR of 8.82 without craniotomy. Compared to some typical NIR-II probes, the developed Er-based NIR-IIb nanoprobes have the following advantages. First, the probes possess a longer emission wavelength than small molecule dyes. This characteristic significantly reduces scattering in biological tissues, leading to an improved signal-to-noise ratio in imaging. Second, the probes are free from heavy metals and exhibit strong emission stability, rendering them more biocompatible

https://doi.org/10.1021/acs.nanolett.3c03698
Nano Lett. 2023, 23, 11203−11210

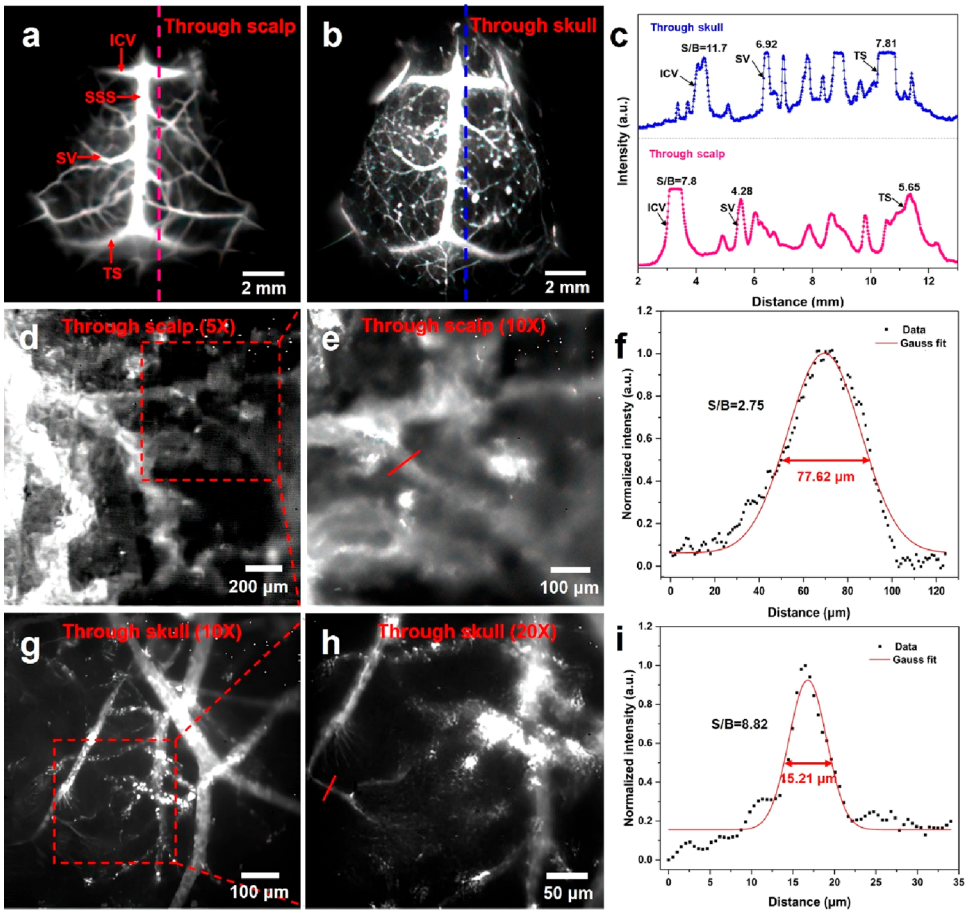

Figure 5. (a, b) NIR-IIb images of whole mouse head through scalp/skull. (c) SBR analysis of NIR-IIb cerebrovascular images in panels (a, b) through cross-sectional intensity profile plots. (d, e) Cerebral vascular image of the same mouse head through scalp, taken using 5X and 10X microscope objectives. (f) Cross-sectional luminescence intensity profiles (black) and Gauss fit (red) along the red-dashed bars in (e) Cerebral vascular image of the same mouse head through skull, taken using 10× and 20× microscope objectives. (i) Cross-sectional luminescence intensity profiles (black) and Gauss fit (red) along the red-dashed bars in h.

than other nanoparticles such as quantum dots or carbon dots. Diverging from prior research on lanthanide nanoparticles for NIR-II imaging, we have optimized the sensitizer content of the probes through a core−shell−shell structure. This enhances excitation content while regulating the nanoparticle size.[37−40] Additionally, the use of liposomes to encapsulate the probes further accelerates their metabolism in living organisms, making them more suitable for intravital imaging. However, the current study only focuses on imaging of cerebrovascular vessels and does not target any specific objects. In future studies, we aim to modify the ligands on the surface of liposomes to enable specific imaging of biological processes in the brain or in other preclinical animal models with high spatial and temporal resolution, thereby making significant progress in the field of in vivo optical imaging.

■ ASSOCIATED CONTENT

Supporting Information

The Supporting Information is available free of charge at https://pubs.acs.org/doi/10.1021/acs.nanolett.3c03698.

Experimental methods, including materials and reagents, as well as detailed procedures; transmission electron microscopy, X-ray diffraction, energy-dispersive X-ray mapping, luminescence emission spectra, absorbance spectra, and lifetime measurements of synthesized nanoparticles; size distribution, zeta potential, photostability, and safety validation of the nanoparticles after liposome encapsulation; NIR-II images of microvascular and vital organs, isolated organ images, images stained with hematoxylin and eosin, profiles of blood chemistry, and validation of imaging performance in vitro (PDF)

■ AUTHOR INFORMATION

Corresponding Authors

Junle Qu − *Key Laboratory of Optoelectronic Devices and Systems of Ministry of Education and Guangdong Province, College of Physics and Optoelectronic Engineering, Shenzhen University, Shenzhen 518060, China*; Email: jlqu@szu.edu.cn

Bin Yu − *Key Laboratory of Optoelectronic Devices and Systems of Ministry of Education and Guangdong Province, College of Physics and Optoelectronic Engineering, Shenzhen University, Shenzhen 518060, China*; orcid.org/0000-0002-8698-0155; Email: yubin@szu.edu.cn

Huiqun Cao − *College of Chemistry and Environmental Engineering, Shenzhen University, Shenzhen 518060, China*; Email: chq0524@163.com

https://doi.org/10.1021/acs.nanolett.3c03698
Nano Lett. 2023, 23, 11203−11210

Authors

Rong Xu − *Key Laboratory of Optoelectronic Devices and Systems of Ministry of Education and Guangdong Province, College of Physics and Optoelectronic Engineering, Shenzhen University, Shenzhen 518060, China*

Jiantao Liu − *Key Laboratory of Optoelectronic Devices and Systems of Ministry of Education and Guangdong Province, College of Physics and Optoelectronic Engineering, Shenzhen University, Shenzhen 518060, China*

Danying Lin − *Key Laboratory of Optoelectronic Devices and Systems of Ministry of Education and Guangdong Province, College of Physics and Optoelectronic Engineering, Shenzhen University, Shenzhen 518060, China;* orcid.org/0000-0002-9121-1916

Xian Chen − *Shenzhen Key Laboratory of New Information Display and Storage Materials, College of Materials Science and Engineering, Shenzhen University, Shenzhen 518060, China*

Fuhong Han − *Key Laboratory of Optoelectronic Devices and Systems of Ministry of Education and Guangdong Province, College of Physics and Optoelectronic Engineering, Shenzhen University, Shenzhen 518060, China*

Xiaoyu Weng − *Key Laboratory of Optoelectronic Devices and Systems of Ministry of Education and Guangdong Province, College of Physics and Optoelectronic Engineering, Shenzhen University, Shenzhen 518060, China*

Yiping Wang − *Key Laboratory of Optoelectronic Devices and Systems of Ministry of Education and Guangdong Province, College of Physics and Optoelectronic Engineering, Shenzhen University, Shenzhen 518060, China*

Liwei Liu − *Key Laboratory of Optoelectronic Devices and Systems of Ministry of Education and Guangdong Province, College of Physics and Optoelectronic Engineering, Shenzhen University, Shenzhen 518060, China;* orcid.org/0000-0002-4593-665X

Complete contact information is available at: https://pubs.acs.org/10.1021/acs.nanolett.3c03698

Author Contributions

The paper was written through contributions of all authors. All authors have given approval to the final version of the manuscript. R.X. prepared nanoparticles, biological samples, and wrote the manuscript. J.T.L. performed NIR-II imaging system. F.H.H. analyzed the data. H.Q.C., D.Y.L., X.C, X.Y.W, Y.P.W., L.W.L., B.Y., and J.L.Q. supervised the project.

Notes

The authors declare no competing financial interest.

■ ACKNOWLEDGMENTS

This work has been partially supported by the National Key Research and Development Program of China (2022YFF0712500); National Natural Science Foundation of China (62175166, 62235007, 62022059); Shenzhen Science and Technology Program (JCYJ20200109105411133, JCYJ20220818100202005); Shenzhen Key Laboratory of Photonics and Biophotonics (ZDSYS20210623092006020)

■ REFERENCES

(1) Zhong, Y. T.; Ma, Z. R.; Zhu, S. J.; Yue, J. Y.; Zhang, M. X.; Antaris, A. L.; Yuan, J.; Cui, R.; Wan, H.; Zhou, Y.; et al. Boosting the Down-shifting Luminescence of Rare-earth Nanocrystals for Biological Imaging Beyond 1500 nm. *Nat. Commun.* **2017**, *8*, 737.

(2) Liang, L.; Feng, Z.; Zhang, Q.; Cong, T. D.; Wang, Y.; Qin, X.; Yi, Z.; Ang, M. J. Y.; Zhou, L.; Feng, H.; Xing, B.; Gu, M.; Li, X.; Liu, X. Continuous-Wave Near-Infrared Stimulated-Emission Depletion Microscopy Using Downshifting Lanthanide Nanoparticles. *Nat. Nanotechnol.* **2021**, *16* (9), 975−980.

(3) Diao, S.; Blackburn, J. L.; Hong, G.; Antaris, A. L.; Chang, J.; Wu, J. Z.; Zhang, B.; Cheng, K.; Kuo, C. J.; Dai, H. Fluorescence Imaging In Vivo at Wavelengths beyond 1500 nm. *Angew. Chem., Int. Ed.* **2015**, *54* (49), 14758−14762.

(4) Golovynskyi, S.; Golovynska, I.; Stepanova, L. I.; Datsenko, O. I.; Liu, L.; Qu, J.; Ohulchanskyy, T. Y. Optical Windows for Head Tissues in Near-Infrared and Short-Wave Infrared Regions: Approaching Transcranial Light Applications. *J. Biophotonics* **2018**, *11* (12), e201800141.

(5) Wang, F. F.; Qu, L. Q.; Ren, F. Q.; Baghdasaryan, A.; Jiang, Y. Y.; Hsu, R.; Liang, P.; Li, J. C.; Zhu, G. Z.; Ma, Z. R.; Dai, H. J. High-Precision Tumor Resection Down to Few-Cell Level Guided by NIR-IIb Molecular Fluorescence Imaging. *Proc. Natl. Acad. Sci. U.S.A.* **2022**, *119* (15), e2123111119.

(6) Li, C.; Li, W.; Liu, H.; Zhang, Y.; Chen, G.; Li, Z.; Wang, Q. An Activatable NIR-II Nanoprobe for In Vivo Early Real-Time Diagnosis of Traumatic Brain Injury. *Angew. Chem., Int. Ed.* **2020**, *59* (1), 247−252.

(7) Hong, G.; Diao, S.; Chang, J.; Antaris, A. L.; Chen, C.; Zhang, B.; Zhao, S.; Atochin, D. N.; Huang, P. L.; Andreasson, K. I.; Kuo, C. J.; Dai, H. Through-Skull Fluorescence Imaging of the Brain in A New Near-Infrared Window. *Nat. Photonics* **2014**, *8* (9), 723−730.

(8) Yang, H.; Huang, H.; Ma, X.; Zhang, Y.; Yang, X.; Yu, M.; Sun, Z.; Li, C.; Wu, F.; Wang, Q. Au-Doped Ag_2Te Quantum Dots with Bright NIR-IIb Fluorescence for In Situ Monitoring of Angiogenesis and Arteriogenesis in a Hindlimb Ischemic Model. *Adv. Mater.* **2021**, *33* (37), 2103953.

(9) Li, C. Y.; Chen, G. C.; Zhang, Y. J.; Wu, F.; Wang, Q. B. Advanced Fluorescence Imaging Technology in the Near-Infrared-II Window for Biomedical Applications. *J. Am. Chem. Soc.* **2020**, *142* (35), 14789−14804.

(10) Lu, H.; Carroll, G. M.; Neale, N. R.; Beard, M. C. J. A. N. Infrared Quantum Dots: Progress, Challenges, and Opportunities. *ACS Nano* **2019**, *13* (2), 939−953.

(11) Huang, J.; Li, J.; Lyu, Y.; Miao, Q.; Pu, K. Molecular Optical Imaging Probes for Early Diagnosis of Drug-Induced Acute Kidney Injury. *Nat. Mater.* **2019**, *18* (10), 1133−1143.

(12) Zhang, Q.; Yu, P.; Fan, Y.; Sun, C.; He, H.; Liu, X.; Lu, L.; Zhao, M.; Zhang, H.; Zhang, F. Bright Stable NIR-II J-Aggregated AIE Dibodipy-Based Fluorescent Probe for Dynamic In Vivo Bioimaging. *Angew. Chem., Int. Ed.* **2021**, *60* (8), 3967−3973.

(13) Sun, Z.; Huang, H.; Zhang, R.; Yang, X.; Yang, H.; Li, C.; Zhang, Y.; Wang, Q. Activatable Rare Earth Near-Infrared-II Fluorescence Ratiometric Nanoprobes. *Nano Lett.* **2021**, *21* (15), 6576−6583.

(14) Yang, H. C.; Li, R. F.; Zhang, Y. J.; Yu, M. X.; Wang, Z.; Liu, X.; You, W. W.; Tu, D. T.; Sun, Z. Q.; Zhang, R.; Chen, X. Y.; Wang, Q. B. Colloidal Alloyed Quantum Dots with Enhanced Photoluminescence Quantum Yield in the NIR-II Window. *J. Journal of American Chemical Society* **2021**, *143* (6), 2601−2607.

(15) Sun, T. Y.; Li, Y. H.; Ho, W. L.; Zhu, Q.; Chen, X.; Jin, L. M.; Zhu, H. M.; Huang, B. L.; Lin, J.; Little, B. E.; et al. Integrating Temporal and Spatial Control of Electronic Transitions for Bright Multiphoton Upconversion. *Nat. Commun.* **2019**, *10*, 1811.

(16) Liu, Z.; Ren, F.; Zhang, H.; Yuan, Q.; Jiang, Z.; Liu, H.; Sun, Q.; Li, Z. Boosting often Overlooked Long Wavelength Emissions of Rare-Earth Nanoparticles for NIR-II Fluorescence Imaging of Orthotopic Glioblastoma. *Biomaterials* **2019**, *219*, 119364.

(17) Xia, F.; Gevers, M.; Fognini, A.; Mok, A. T.; Li, B.; Akbari, N.; Zadeh, I. E.; Qin-Dregely, J.; Xu, C. Short-Wave Infrared Confocal Fluorescence Imaging of Deep Mouse Brain with a Superconducting Nanowire Single-Photon Detector. *Acs Photonics* **2021**, *8* (9), 2800−2810.

(18) Huang, D.; Wang, Q.; Cao, Y.; Yang, H.; Li, M.; Wu, F.; Zhang, Y.; Chen, G.; Wang, Q. Multiscale NIR-II Imaging-Guided Brain-Targeted Drug Delivery Using Engineered Cell Membrane Nanoformulation for Alzheimer's Disease Therapy. *ACS Nano* **2023**, *17* (5), 5033−5046.
(19) Wang, F.; Han, Y.; Lim, C. S.; Lu, Y. H.; Wang, J.; Xu, J.; Chen, H. Y.; Zhang, C.; Hong, M. H.; Liu, X. G. Simultaneous Phase and Size Control of Upconversion Nanocrystals Through Lanthanide Doping. *Nature* **2010**, *463* (7284), 1061−1065.
(20) Yan, Y. C.; Faber, A. J.; Dewaal, H. Luminescence Quenching by OH Groups in Highly Er-Doped Phosphate-Glasses. *J. Non-Cryst. Solids* **1995**, *181* (3), 283−290.
(21) Wang, F.; Deng, R. R.; Liu, X. G. Preparation of Core-Shell $NaGdF_4$ Nanoparticles Doped with Luminescent Lanthanide Ions to be Used as Upconversion-Based Probes. *Nat. Protoc.* **2014**, *9* (7), 1634−1644.
(22) Huang, J.; Chen, Y.; Lin, Y.; Gong, X.; Luo, Z.; Huang, Y. Enhanced Efficiency of Er:Yb:Ce:$NaGd(WO_4)^2$ Laser at 1.5−1.6 Microm by the Introduction of High-Doping Ce^{3+} Ions. *Opt. Lett.* **2008**, *33* (21), 2548−50.
(23) Zheng, B.; Fan, J.; Chen, B.; Qin, X.; Wang, J.; Wang, F.; Deng, R.; Liu, X. Rare-Earth Doping in Nanostructured Inorganic Materials. *Chem. Rev.* **2022**, *122* (6), 5519−5603.
(24) Wen, H. L.; Zhu, H.; Chen, X.; Hung, T. F.; Wang, B. L.; Zhu, G. Y.; Yu, S. F.; Wang, F. Upconverting Near-Infrared Light through Energy Management in Core-Shell-Shell Nanoparticles. *Angew. Chem., Int. Ed.* **2013**, *52* (50), 13419−13423.
(25) Zhong, Y. T.; Ma, Z. R.; Wang, F. F.; Wang, X.; Yang, Y. J.; Liu, Y. L.; Zhao, X.; Li, J. C.; Du, H. T.; Zhang, M. X.; Cui, Q. H.; Zhu, S. J.; Sun, Q. C.; Wan, H.; Tian, Y.; Liu, Q.; Wang, W. Z.; Garcia, K. C.; Dai, H. J. In Vivo Molecular Imaging for Immunotherapy Using Ultra-bright Near-Infrared-IIb Rare-Earth Nanoparticles. *Nat. Biotechnol.* **2019**, *37* (11), 1322−1331.
(26) Yi, G. S.; Chow, G. M. Water-Soluble $NaYF_4$: Yb,Er(Tm)/$NaYF_4$/Polymer Core/Shell/Shell Nanoparticles with Significant Enhancement of Upconversion Fluorescence. *Chem. Mater.* **2007**, *19* (3), 341−343.
(27) Wang, P.; Fan, Y.; Lu, L.; Liu, L.; Fan, L.; Zhao, M.; Xie, Y.; Xu, C.; Zhang, F. NIR-II Nanoprobes in-Vivo Assembly to Improve Image-Guided Surgery for Metastatic Ovarian Cancer. *Nat. Commun.* **2018**, *9* (1), 2898.
(28) Chen, Y.; Wang, S.; Zhang, F. Near-Infrared Luminescence High-Contrast in Vivo Biomedical Imaging. *Nature Reviews Bioengineering* **2023**, *1* (1), 60−78.
(29) Zhao, M.; Sik, A.; Zhang, H.; Zhang, F. Tailored NIR-II Lanthanide Luminescent Nanocrystals for Improved Biomedical Application. *Adv. Opt. Mater.* **2023**, *11* (11), 2002039.
(30) Remaut, K.; Lucas, B.; Braeckmans, K.; Demeester, J.; De Smedt, S. C. Pegylation of Liposomes Favours the Endosomal Degradation of the Delivered Phosphodiester Oligonucleotides. *J. Controlled Release* **2007**, *117* (2), 256−266.
(31) Liu, Z.; Davis, C.; Cai, W. B.; He, L.; Chen, X. Y.; Dai, H. J. Circulation and Long-term Fate of Functionalized, Biocompatible Single-Walled Carbon Nanotubes in Mice Probed by Raman Spectroscopy. *Proc. Natl. Acad. Sci. U.S.A.* **2008**, *105* (5), 1410−1415.
(32) Kim, J. Y.; Kim, J. K.; Park, J. S.; Byun, Y.; Kim, C. K. The Use of PEGylated Liposomes to Prolong Circulation Lifetimes of Tissue Plasminogen Activator. *Biomaterials* **2009**, *30* (29), 5751−5756.
(33) He, S.; Chen, S.; Li, D.; Wu, Y.; Zhang, X.; Liu, J.; Song, J.; Liu, L.; Qu, J.; Cheng, Z. High Affinity to Skeleton Rare Earth Doped Nanoparticles for Near-Infrared II Imaging. *Nano Lett.* **2019**, *19* (5), 2985−2992.
(34) Li, D.; He, S.; Wu, Y.; Liu, J.; Liu, Q.; Chang, B.; Zhang, Q.; Xiang, Z.; Yuan, Y.; Jian, C.; et al. Excretable Lanthanide Nanoparticle for Biomedical Imaging and Surgical Navigation in the Second Near-Infrared Window. *Adv. Sci.* **2019**, *6* (23), 1902042.
(35) Horton, N. G.; Wang, K.; Kobat, D.; Clark, C. G.; Wise, F. W.; Schaffer, C. B.; Xu, C. In Vivo Three-photon Microscopy of Subcortical Structures Within an Intact Mouse Brain. *Nat. Photonics* **2013**, *7* (3), 205−209.
(36) Zheng, T.; Wang, W. T.; Ashley, J.; Zhang, M.; Feng, X. T.; Shen, J.; Sun, Y. Self-Assembly Protein Superstructures as a Powerful Chemodynamic Therapy Nanoagent for Glioblastoma Treatment. *Nano-Micro Letters* **2020**, *12* (1), 151.
(37) Li, H.; Wang, X.; Li, X.; Zeng, S.; Chen, G. Clearable Shortwave-Infrared-Emitting $NaErF_4$ Nanoparticles for Noninvasive Dynamic Vascular Imaging. *Chem. Mater.* **2020**, *32* (8), 3365−3375.
(38) Wang, X.; Yakovliev, A.; Ohulchanskyy, T. Y.; Wu, L.; Zeng, S.; Han, X.; Qu, J.; Chen, G. Efficient Erbium-Sensitized Core/Shell Nanocrystals for Short Wave Infrared Bioimaging. *Adv. Opt. Mater.* **2018**, *6* (20), 1800690.
(39) Wang, W.; Feng, Z.; Li, B.; Chang, Y.; Li, X.; Yan, X.; Chen, R.; Yu, X.; Zhao, H.; Lu, G.; Kong, X.; Qian, J.; Liu, X. Er^{3+} Self-Sensitized Nanoprobes with Enhanced 1525 nm Downshifting Emission for NIR-IIb in Vivo Bio-imaging. *J. Mater. Chem. B* **2021**, *9* (12), 2899−2908.
(40) Rajagopalan, K.; Madirov, E.; Busko, D.; Howard, I. A.; Richards, B. S.; Swart, H. C.; Turshatov, A. High Quantum Yield Shortwave Infrared Luminescent Tracers for Improved Sorting of Plastic Waste. *ACS Appl. Mater. Interfaces* **2023**, *15* (37), 43985−43993.

https://doi.org/10.1021/acs.nanolett.3c03698
Nano Lett. 2023, 23, 11203−11210